NiO_x Electrode Interlayer and $CH_3NH_2/CH_3NH_3PbBr_3$ Interface Treatment to Markedly Advance Hybrid Perovskite-Based Light-Emitting Diodes

*Yi-Kai Chih, Jian-Chih Wang, Rei-Ting Yang, Chi-Ching Liu, Yun-Chorng Chang, Yaw-Shyan Fu, Wei-Chi Lai, Peter Chen, Ten-Chin Wen, Yu-Ching Huang, Cheng-Si Tsao, and Tzung-Fang Guo**

Chondroudis and Mitzi first reported the room-temperature electroluminescence (EL) from the hybrid organic–inorganic perovskite-based light-emitting diodes (LED).[1,2] The device configuration employed a quartz/indium-tin-oxide (ITO) substrate, $(H_3NC_2H_4C_{16}H_8S_4C_2H_4NH_3)PbCl_4$, 1,3-bis[4-(tert-butylphenyl)-1,3,4-oxadiazolyl]phenylene, and MgAg as the device anode, light-emissive layer, electron transport layer, and cathode, respectively. The hybrid LED turned on at 5.5 V and emitted a bright green EL around 530 nm. Chondroudis and Mitzi's work successfully incorporated organic–inorganic perovskite materials as the light-emissive layer with the typical device configuration for organic light-emitting diodes (OLEDs).[1,2] Accordingly, well-established techniques could be utilized for fabricating highly efficient OLEDs within the past two decades, such as vacuum thermal deposition of thin films, the application of various types of organic/inorganic charge injection, transport, blocking layers, new design of the device structure, etc., to advance the performance of perovskite-based LEDs.[3–12]

Dr. Y.-K. Chih, J.-C. Wang, R.-T. Yang, Prof. W.-C. Lai, Prof. P. Chen, Prof. T.-F. Guo
Department of Photonics
National Cheng Kung University
Tainan, Taiwan 701 ROC
E-mail: guotf@mail.ncku.edu.tw
C.-C. Liu, Prof. Y.-C. Chang
Research Center for Applied Science
Academia Sinica
Taipei, Taiwan 115
Prof. Y.-S. Fu
Department of Greenergy Technology
National University of Tainan
Tainan, Taiwan 701
Prof. W.-C. Lai, Prof. T.-F. Guo
Advanced Optoelectronic Technology Center
National Cheng Kung University
Tainan, Taiwan 701
Prof. T.-C. Wen
Department of Chemical Engineering
National Cheng Kung University
Tainan, Taiwan 701
Dr. Y.-C. Huang, Dr. C.-S. Tsao
Institute of Nuclear Energy Research
Atomic Energy Council
Taoyuan, Taiwan 325

DOI: 10.1002/adma.201602974

Cho et al. had boosted the current efficiency of perovskite-based LEDs to 42.9 cd A^{-1} by a nanocrystal pinning (NCP) method.[13] Dropping the chloroform solvent on top of the wet precursor layer during the spinning coating process induces the fast crystallization of perovskite film. Cho et al. obtained a nicely covered $CH_3NH_3PbBr_3$ polycrystalline thin film by an NCP method on the substrate of a well-packed assembly of tiny grains ranging from 100 to 250 nm. The tiny grains in Cho et al.'s work form a very dense and flat perovskite film, reducing the pinholes, the bad interface causing the electric shunt paths in fabricating devices. Additionally, the tiny grains may confine the exciton diffusion, reduce the exciton dissociation into carriers, and increase the luminescent properties.[13] Although Cho et al. had demonstrated the hybrid perovskite LEDs of highest performance by NCP method up to date, considering to further elevate LED parameters in the next step of research, the high densities of grain boundaries (surface states) among tiny grain interfaces in the polycrystalline perovskite film possibly trap the charges, are the defects and nonradiative recombination centers to degrade the device performance.

Many reported approaches that can effectively improve the morphologies of polycrystalline perovskite film in fabricating hybrid perovskite-based photovoltaic cells may not be applicable to prepare $CH_3NH_3PbBr_3$ layer for LED applications.[14–23] The coarsening of the $CH_3NH_3PbBr_3$ film forms a nonuniform distribution of many large cuboid crystals on the substrate.[9,24–26] This could generate voids between the grains, which results in shunting of the device through direct contact of positive and negative electrodes. Other attempts by incorporating the conjugated or insulating polymers with $CH_3NH_3PbBr_3$ polycrystalline film or nanocrystals enhanced the brightness and efficiency of perovskite-based LEDs,[3,8,9,24–27] but the polymer might increase the series resistance of devices during the operation. Sometimes, we also observed the "twinkling" emission of EL on the pixel from $CH_3NH_3PbBr_3$ crystals.[25,27] Presumably, the preparation of the densely packed $CH_3NH_3PbBr_3$ polycrystalline film of controllable crystal domains, grain sizes, defects, boundaries, compositions, etc., would still be the key parameters to dominate the device output performance.[13]

Recent studies reported that the instant exposure of $CH_3NH_3PbI_3$ crystals or polycrystalline film to methylamine (CH_3NH_2, MA) gas atmosphere at room temperature forms a liquid-phase $CH_3NH_3PbI_3 \bullet x$MA intermediate layer on the substrate.[28–36] Basically, it is a unique gas–solid interaction to dissolve $CH_3NH_3PbI_3$ perovskite by MA gas.[29–34] Later,

the regrowth of $CH_3NH_3PbI_3$ by degasing MA in ambient environment forms a compact and flat polycrystalline thin film of proper crystal morphologies, and markedly improves the photovoltaic parameters.[29–36] These works imply that MA treatment may "heal" the voids and pinholes of perovskite film as prepared by the spin coating process. In other words, the post-treatment by MA gas could possibly reconstruct the morphology of $CH_3NH_3PbBr_3$ film. It is also noted that delicate dynamic control of the MA treatment is required to ensure the morphologies of $CH_3NH_3PbBr_3$ film suitable for LED applications.

In this manuscript, we present the efficient $CH_3NH_3PbBr_3$-based hybrid LED of a brightness >70 000 cd m^{-2} and the luminous efficiency (LE) >15 cd A^{-1}. First, the commonly used poly(3,4-ethylenedioxythiophene) poly(styrene-sulfonate) (PEDOT:PSS) hole transport layer (HTL) has to be replaced by a more suitable electrode interlayer, a compact nickel oxide (NiO_x) layer.[37–44] The NiO_x electrode interlayer helps the formation of a shiny $CH_3NH_3PbBr_3$ film on the substrate, exhibits a suitable energy level for the transport of holes, and also to some extent blocks the transport of the electrons in $CH_3NH_3PbBr_3$ reaching the electrodes to increase the probabilities for the recombination of opposite charge carriers in the active layer. Second, we successfully apply a moderate gas–solid reaction to treat $CH_3NH_3PbBr_3$ film. A mild process (under a low MA atmosphere for 60–80 s at room temperature) significantly advances the quality, the crystallinity, photoluminescence (PL) of the perovskite films and endorses a more than 100-fold increase in brightness and LE as compared to those of the controlled cell without MA-treatment. A hybrid perovskite-based LED with the simple configuration of glass/ITO/NiO_x/MA treated $CH_3NH_3PbBr_3$/1,3,5-tris(1-phenyl-1H-benzimidazol-2-yl)benzene (TPBI)/LiF/Al, exhibits a peak LE of 15.9 cd A^{-1} biased at 8.50 V, 407.65 mA cm^{-2}, 65 300 cd m^{-2}, posing a feasible gas–solid interaction to largely improve the performance and the design of the highly bright and efficient perovskite-based LEDs for real applications.

Many studies had reported $CH_3NH_3PbI_3$ polycrystalline film changes its color (bleaching) immediately while exposing to amine or MA vapor at room temperature and then turns dark again within few seconds by removing it from amine or MA atmosphere.[28,29,32–34] The whole process is a fast and reversible gas–solid interaction. Generally speaking, the drastic transformation between liquid intermediate with solid phases in such short period of time may not be suitable to reconstruct the morphologies of polycrystalline film. As a result, we apply a solid reaction to generate MA gas mildly and to treat $CH_3NH_3PbBr_3$ polycrystalline film at a relatively slow interaction rate. **Figure 1** presents the schematic draw illustrating Step 1, the process to prepare $CH_3NH_3PbBr_3$ polycrystalline film, and Step 2, the setup to generate MA gas for MA-$CH_3NH_3PbBr_3$ gas–solid reaction. In Step 1, we applied the similar NCP method as reported by Cho et al. by dropping 500 µL chloroform solvent on surface of the precursor film at 60 s during the spin coating.[13] This process induces the fast crystallization and forms a shiny and flat surface of perovskite layer on glass/ITO/NiO_x substrate. In Step 2, we adopt a solid reaction to directly blend $CH_3NH_3Cl_{(s)}$ with $KOH_{(s)}$ powders in a small vial (4 mL). $CH_3NH_3Cl_{(s)}$ reacts slowly with $KOH_{(s)}$ to generate $MA_{(g)}$, $KCl_{(s)}$, and $H_2O_{(l)}$ at room temperature. Another big vial (50 mL) contains $CaO_{(s)}$ desiccant to absorb H_2O in the above reaction. The glass/ITO/NiO_x/$CH_3NH_3PbBr_3$ substrate is placed upside down in the big vial to react with MA gas coming out from the bottom.

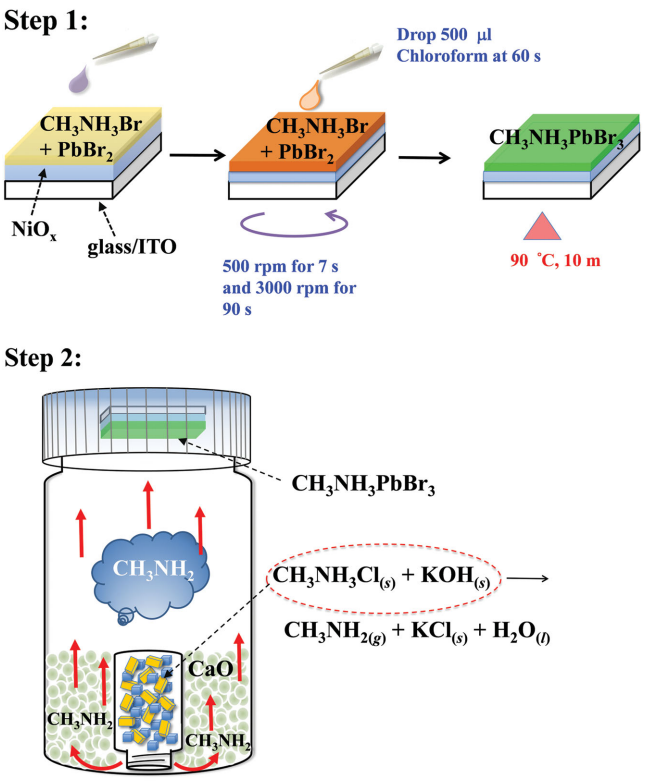

Figure 1. The schematic drawing illustrates Step 1, the process to prepare $CH_3NH_3PbBr_3$ polycrystalline film, and Step 2, the setup to generate MA gas for MA-$CH_3NH_3PbBr_3$ gas–solid reaction. In Step 1, 500 µL chloroform solvent was dropped on the surface of the precursor film at 60 s during the spin coating. In Step 2, $CH_3NH_3Cl_{(s)}$ was directly blended with with $KOH_{(s)}$ powder in a small vial (4 mL). $CH_3NH_3Cl_{(s)}$ reacted slowly with $KOH_{(s)}$ to generate $MA_{(g)}$, $KCl_{(s)}$, and $H_2O_{(l)}$ at room temperature. Another large vial (50 mL) contained $CaO_{(s)}$ desiccant to absorb H_2O in the above reaction. The glass/ITO/NiO_x/$CH_3NH_3PbBr_3$ substrate was placed upside down in the large vial to react with MA gas expelled from the bottom.

In our study, $CH_3NH_3PbBr_3$ film completely changes its color from green yellow to colorless by ≈150 to 180 s of exposure to MA atmosphere (Step 2 in Figure 1). This observation infers that the reaction rate as depicted in Step 2 to generate MA gas is moderate and the gas–solid interaction between MA with $CH_3NH_3PbBr_3$ is relatively slow as compared to previous reports published elsewhere (color changed within seconds).[28,29,32–34] However, after removing the substrate from the vial (MA atmosphere) to ambient at room temperature, $CH_3NH_3PbBr_3$ film instantly turns back green yellow color. This result indicates that MA treatment takes few minutes to completely transfer the solid-phase $CH_3NH_3PbBr_3$ to liquid-phase $CH_3NH_3PbBr_3$•xMA intermediate in our work, but the degasing of MA from liquid-phase $CH_3NH_3PbBr_3$•xMA intermediate can be done within seconds in ambient environment. **Figure 2**a shows the scanning electron microscopy (SEM)

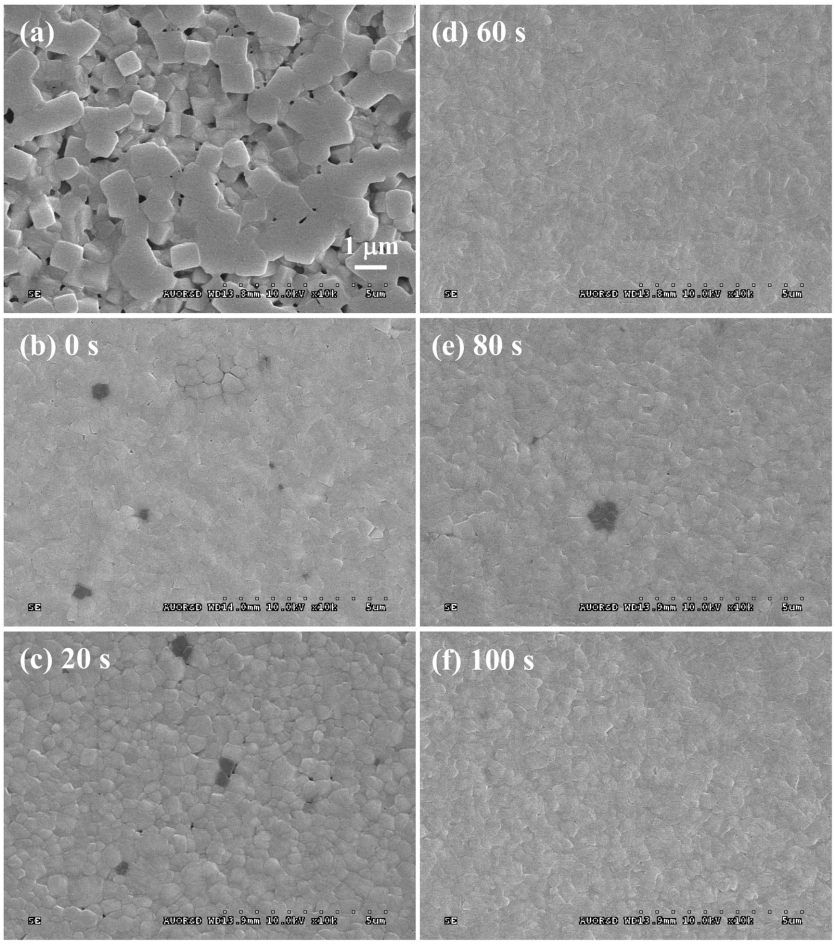

Figure 2. SEM images of glass/ITO/NiO_x/$CH_3NH_3PbBr_3$ samples with different MA treatment time a) 180 s, b) 0 s, c) 20 s, d) 60 s, e) 80 s, and f) 100 s.

image of $CH_3NH_3PbBr_3$ film after 180 s of MA treatment. We observe the formation of many large cuboid crystals (around 1 μm size) on the substrate. The $CH_3NH_3PbBr_3$ film is not uniformly covered on the substrate with many voids between grains. We note that rapid transformation of a liquid-phase $CH_3NH_3PbBr_3$•*x*MA intermediate back to $CH_3NH_3PbBr_3$ phase coarsens the film and changes the morphology radically, in which the quality of $CH_3NH_3PbBr_3$ film is not suitable for fabricating decent cells. Accordingly, this result implies that the correct procedure for MA treatment is around the time prior to the complete transformation of $CH_3NH_3PbBr_3$ film (solid) to the liquid-phase $CH_3NH_3PbBr_3$•*x*MA intermediate.

Figure 2 presents the SEM images of glass/ITO/NiO_x/$CH_3NH_3PbBr_3$ samples with different MA treatment time. Figure 2b illustrates SEM image for $CH_3NH_3PbBr_3$ sample without MA treatment (0 s). The film is uniformly coated on the substrate and is composed of many tiny grains, agreeing with the previous report of $CH_3NH_3PbBr_3$ film prepared by a similar NCP method. After exposing the film to MA gas for 20 s, as shown in Figure 2c, the crystal boundaries are visible on the surface of the $CH_3NH_3PbBr_3$ polycrystalline film. The average grain sizes in Figure 2c are smaller than 0.5 μm. The result indicates that 20 s MA treatment is quite effective for the gas–solid reaction in the grain boundaries, but it did not drastically change the film morphology as compared to the SEM image without MA treatment in Figure 2b. Figure 2d–f is SEM images of $CH_3NH_3PbBr_3$ films treated at 60, 80, and 100 s, respectively, exhibiting the similar surface morphology of a densely packed and covered film on the substrate. It is also worth noting that there is a transformation in SEM images at the grain boundaries as shown in Figure 2c,d. The boundary interfaces become unclear in Figure 2d–f as compared to those in Figure 2c, which infers that the gas–solid reaction initiates the regrowth of $CH_3NH_3PbBr_3$ crystallites through the grain boundaries. Since MA treatment in our study is modulated at 60–100 s of time in a mild condition, the dynamic equilibrium between a liquid-phase $CH_3NH_3PbBr_3$•*x*MA intermediate with solid-phase $CH_3NH_3PbBr_3$ preserves the transformation of $CH_3NH_3PbBr_3$ crystallites in a relatively slow process and forms the uniform coverage of the film on the substrate as characterized by SEM images in Figure 2. Presumably, the reconstruction of $CH_3NH_3PbBr_3$ crystallites would follow the preferred crystal orientations on glass/ITO/NiO_x substrate under the equilibrium and improve the quality of $CH_3NH_3PbBr_3$ polycrystalline film for LED applications.

Figure 3 presents X-ray diffraction (XRD) patterns of $CH_3NH_3PbBr_3$ films at different MA treatment times. The XRD patterns for $CH_3NH_3PbBr_3$ films prepared by NCP method without MA treatment exhibit several peaks, assigned to (100), (110), (200), (210), (211), (220), and (300) planes in the plot. The positions of these peaks fit the results previously published elsewhere.[13,24–27] After 20 s of MA treatment, we observed an approximately twofold to threefold increase in XRD intensity at (100) and (200) peaks. Further increasing MA treatment time markedly enhances (100) and (200) peaks in XRD patterns. The intensities of (100) and (200) peaks for $CH_3NH_3PbBr_3$ film with 80 s MA treatment received a fivefold intensity compared to that without MA treatment. However, as shown in Figure 3, the relative intensity of peaks (110), (210), (211), and (220) to that of peaks (100) and (200) decrease with MA treatment time. These results fortify that the regrowth of $CH_3NH_3PbBr_3$ crystallites by MA treatment prefers the formation of (100) and (200) planes on the substrate.[29,33] A slow process under the equilibrium is favorable to reconstruct the polycrystalline film with the preferred crystal orientation. Notably, the full-width-half-maximum (FWHM) of peak intensity at (100) did not apparently change with MA treatment time, suggesting the minor influence on the average crystal size of $CH_3NH_3PbBr_3$ crystallites herein. This observation is correlated with SEM images as presented in Figure 2b–f. The inset of Figure 3 depicts the water-contact-angle image of glass/ITO/NiO_x substrate, around 10°. The surface of NiO_x electrode

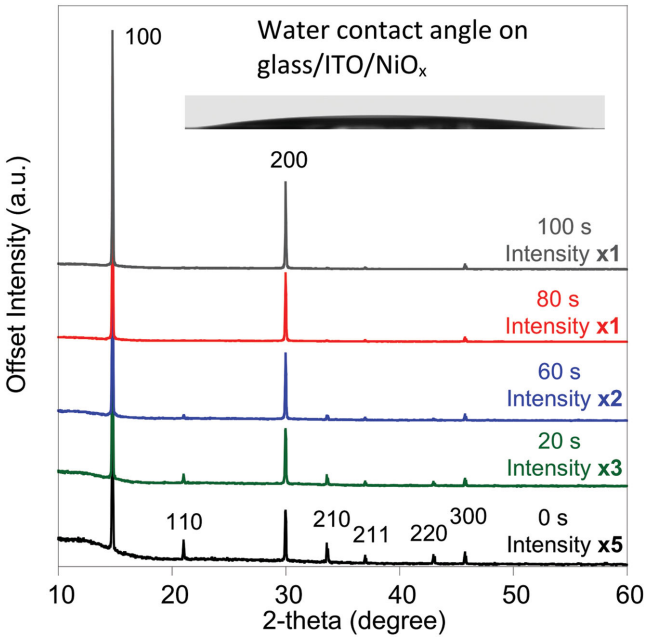

Figure 3. X-ray diffraction (XRD) patterns of $CH_3NH_3PbBr_3$ films at different MA treatment times. The inset presents the image of water contact angle on glass/ITO/NiO_x substrate.

interlayer is hydrophilic to the polar solvent, which possibly promotes the uniform coverage of $CH_3NH_3PbBr_3$ on the substrate and the regrowth of $CH_3NH_3PbBr_3$ crystallites following the preferred direction.

Figure 4a depicts the device configuration, composed of glass/ITO/NiO_x/$CH_3NH_3PbBr_3$/TPBI/LiF/Al and Figure 4b diagrams the energy levels of each layer. As illustrated in Figure 4b, NiO_x exhibits an energy level of 5.30–5.40 eV, a cascade between the work function of ITO with the valence band (VB) edge level of $CH_3NH_3PbBr_3$ for the transport of holes. On the other hand, the energy barriers at VB and conduction band (CB) edge levels of $CH_3NH_3PbBr_3$ with TPBI and NiO_x, respectively, would block the transport of the holes and electrons to reach the electrodes and increase the probabilities for the recombination of opposite charge carriers in $CH_3NH_3PbBr_3$ active layer. It is worth noting that MA treatment may modulate the relative energy levels of $CH_3NH_3PbBr_3$ film. Supporting Information presents the optical absorbance (Figure S1, Supporting Information) and normalized PL spectra (Figure S2, Supporting Information) of $CH_3NH_3PbBr_3$ films on glass/ITO/NiO_x substrates with 0 and 80 s MA treatment. As illustrated in Figure S1 (Supporting Information), the curve shape of the absorbance spectra are basically the same for $CH_3NH_3PbBr_3$ films with 0 and 80 s MA treatment. There is only a difference in the magnitude of absorbance around 350 nm. The result indicates 80 s MA treatment did not induce the compositional transformation of $CH_3NH_3PbBr_3$ perovskite. In Figure S2 (Supporting Information), there is a small red shift (few nm) of PL peak emission by 80 s MA treatment at the normalized PL spectra. We estimate the changes in the relative energy levels of $CH_3NH_3PbBr_3$ film by MA treatment would not be significant to modulate the transport and confinement of charge carriers in the heterojunction interfaces.

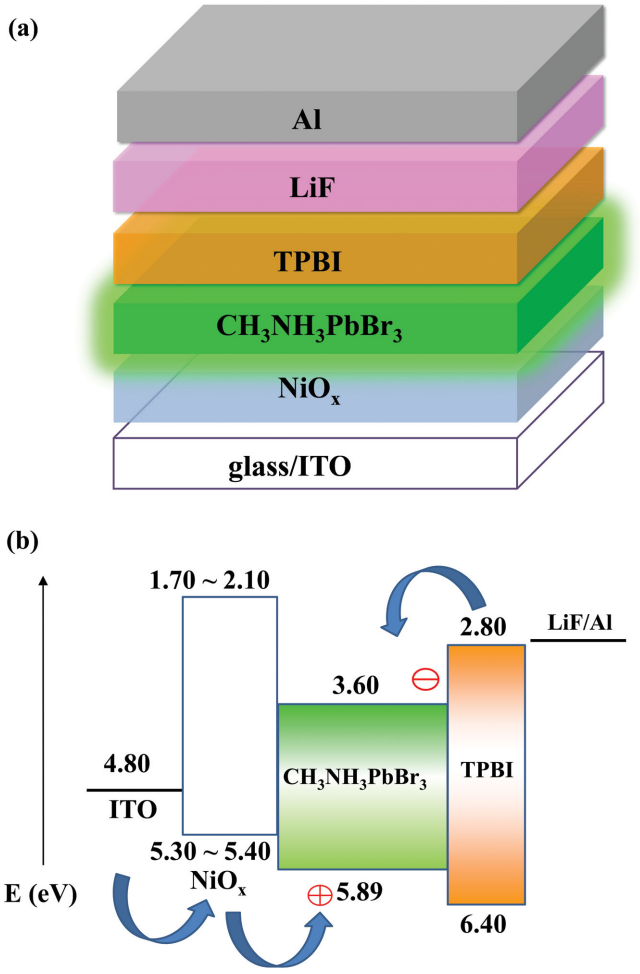

Figure 4. a) The device configuration is composed of glass/ITO/NiO_x/$CH_3NH_3PbBr_3$/TPBI/LiF/Al and b) energy-level diagram of each layer.

Figure 5a presents the current density–brightness–voltage (*J*–*L*–*V*) curves and Figure 5b depicts the LE versus current density curves for the hybrid perovskite-based LEDs in this study. In Figure 5a, the threshold voltage (current) is around 2.5 V for the hybrid LED made of $CH_3NH_3PbBr_3$ layer without MA treatment, and the light turn-on voltage is about 5.8 V. The device has a brightness of 583.0 cd m^{-2} while biased at 9.0 V and a low LE of 0.07 cd A^{-1}. For the device made of $CH_3NH_3PbBr_3$ layer with 20 s MA treatment, the threshold voltage shifts to 2.0 V and light turn-on voltage reduces to below 4.0 V. The device shows a markedly enhanced EL intensity with a brightness of 6670.0 cd m^{-2} and a LE of 3.1 cd A^{-1} biased at 9.0 V. It is also noted that the performance of hybrid LEDs increases with MA treatment time. The cell made of 60 s MA treated $CH_3NH_3PbBr_3$ layer exhibits a brightness of 16 900 cd m^{-2} biased at 9.0 V. For the device with 80 s MA treatment, it has the light turn-on voltage below 4.0 V, a very high EL intensity, larger than 70 000 cd m^{-2} biased at 9.0 V, and a maximal LE of 15.9 cd A^{-1} biased at 8.5 V. Figure S3 (Supporting Information) presents the normalized EL spectrum of the hybrid $CH_3NH_3PbBr_3$ LED of 80 s MA treatment. EL spectrum has the narrow FWHM around 25 nm. However, the prolonged

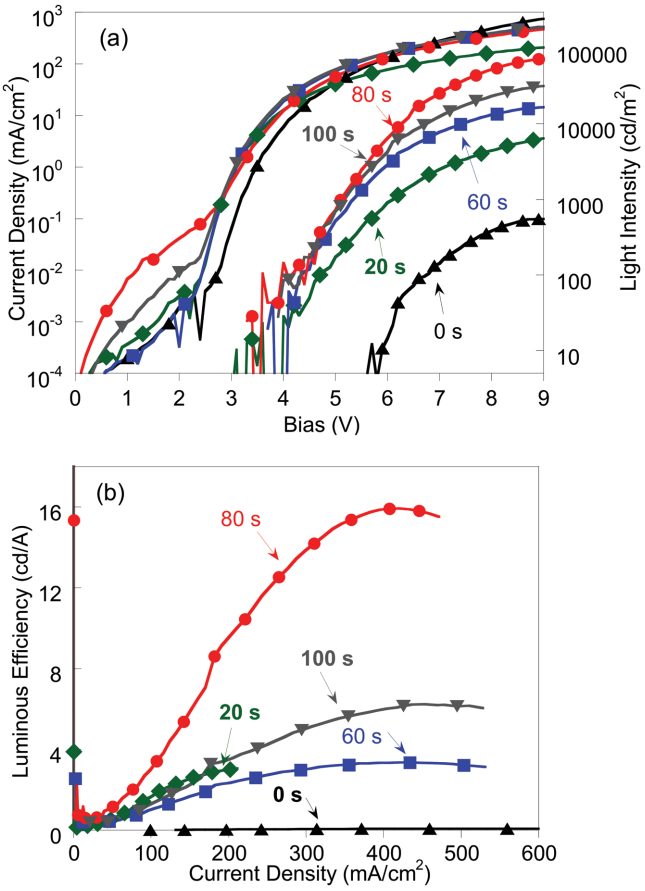

Figure 5. a) The *J–L–V* curves for hybrid LEDs of glass/ITO/NiO_x/$CH_3NH_3PbBr_3$/TPBI/LiF/Al configuration with (▲) 0 s, (◆) 20 s, (■) 60 s, (●) 80 s, and (▼) 100 s MA treatment. b) LE versus current density curves for the hybrid LEDs in (a).

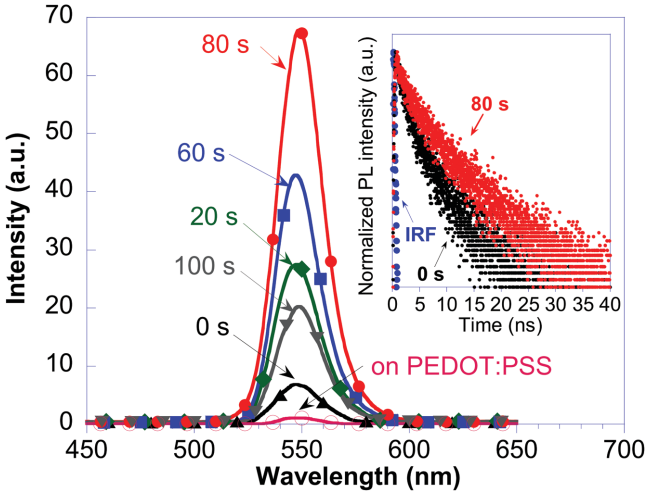

Figure 6. PL spectra of $CH_3NH_3PbBr_3$ films on glass/ITO/NiO_x substrates with (▲) 0 s, (◆) 20 s, (■) 60 s, (●) 80 s, and (▼) 100 s MA treatment. (○) PL spectrum of $CH_3NH_3PbBr_3$ film on glass/ITO/PEDOT:PSS substrate without MA treatment. The inset presents TRPL decay curves for $CH_3NH_3PbBr_3$ films (black dots) without treatment, (red dots) with 80 s MA treatment, and (blue dots) IRF.

MA treatment, 100 s, decreases EL intensity and LE. As characterized by SEM and XRD measurements in Figures 2 and 3, we attribute that MA treatment induces the densely packed morphology of $CH_3NH_3PbBr_3$ polycrystalline film with the preferred crystal orientation on glass/ITO/NiO_x substrate to the enhanced LED performance. The device of 80 s MA treatment is the optimal condition for hybrid LED, herein showing the highest EL brightness and LE as illustrated in Figure 5.

The device performance is also associated with the optical properties of $CH_3NH_3PbBr_3$ films. **Figure 6** illustrates PL measurement of $CH_3NH_3PbBr_3$ films. The PL intensity of $CH_3NH_3PbBr_3$ layer prepared on glass/ITO/PEDOT:PSS substrate is very low as shown in Figure 6.[2,13] The efficient carrier transfer at PEDOT:PSS/$CH_3NH_3PbBr_3$ interface dissociates the excited states, suppresses the recombination of charge carriers, and reduces PL in $CH_3NH_3PbBr_3$ layer. Although PEDOT:PSS had been successfully used as a HTL in efficient perovskite-based hybrid solar cells,[45,46] apparently PEDOT:PSS should not be a suitable HTL material in fabricating $CH_3NH_3PbBr_3$-based hybrid LEDs due to the severe quenching of luminescence in $CH_3NH_3PbBr_3$ perovskite layer. The maximal EL intensity for the hybrid LED applying PEDOT:PSS as the hole transport layer in our study is around 200 cd m^{-2} biased at 12 V and the LE is very low (data not shown here). When to prepare $CH_3NH_3PbBr_3$ on glass/ITO/NiO_x substrate, the energy barrier between CB edge levels of $CH_3NH_3PbBr_3$ with NiO_x, as depicted in Figure 4b, blocks the electron transfer and the recombination of opposite charge carriers in the electrode. As a result, PL intensity relatively increases for $CH_3NH_3PbBr_3$ layer prepared on glass/ITO/NiO_x in comparison with that of film on glass/ITO/PEDOT:PSS substrate. The difference in PL intensity can be seen by the naked eye under the UV lamp irradiation. Additionally, as illustrated in Figure 6, the magnitude of PL constantly increases with MA treatment time from 0 to 80 s. $CH_3NH_3PbBr_3$ film of 80 s MA treatment exhibits a maximal PL intensity, about a tenfold increase than that of the film without MA treatment (0 s). This can be attributed to a better crystal morphology of $CH_3NH_3PbBr_3$ film. However, it is noted that PL intensity is decreased for the film of 100 s MA treatment. We are aware that the film of 100 s MA treatment exhibits a weaker PL, but a better EL intensity and efficiency than those of devices made of perovskite films with 20 and 60 s MA treatment as shown in Figure 5a,b. There are several parameters to modulate the output performance of LEDs, including the balanced injection of opposite charge carriers, the confinement of excited states in the active layer, PL quantum efficiency, number density of defects and voids, the crystal morphology, the film quality of $CH_3NH_3PbBr_3$, etc. We are still studying the fundamental mechanisms, resulting in the modulation of the device performance by MA treatment time. This part of our work is currently under intensive investigation.

The inset of Figure 6 presents the time-resolved PL (TRPL) decay curves for $CH_3NH_3PbBr_3$ films without (0 s) and with 80 s MA treatment. The PL decay curves can be fitted with the biexponential decay model, composed of a fast and a slow decay component corresponding to a short and long lifetime, t_1, t_2, respectively. The t_1 and t_2 are 2.67 ns (parameter A_1: 166.3) and 13.0 ns (A_1: 60.2) for $CH_3NH_3PbBr_3$ film without

MA treatment. After 80 s MA treatment, both t_1 and t_2 increase to 4.97 ns (A_1: 132.1) and 18.54 ns (A_1: 72.2), respectively. The extended TRPL lifetime of the MA-treated sample indicates the suppression of nonradiative decay process, which can be attributed to the reduced defect densities by MA vapor healing processing. The observation in TRPL decay curves might be correlated with the increased PL intensity by MA treatment as illustrated in Figure 6. However, as shown in Figure 5b, LE of the hybrid LEDs gradually increases with the current density and achieves a maximum at the high current regime. The result suggests that the efficiency of the device is still limited by the traps and defects at the grain boundaries and grains/electrode interfaces. The MA treatment method developed in this work is an effective process to improve the quality of $CH_3NH_3PbBr_3$ polycrystalline film (reduce the defect sites). Other than the modifications of thin film microstructures, this facile approach showed a pronounced increase on the performances of the light emitting device. We believe further advances are expected with delicate control on the regrowth process of $CH_3NH_3PbBr_3$ crystallites during MA treatment, such as temperature, atmosphere, flow rate, etc. Currently, optimizations on the aforementioned parameters are under intensive investigations in our group.

In conclusion, the merits of the methods we developed in the paper represent a new paradigm for hybrid perovskite-based LED of a conventional OLED architecture. We report that the commonly used PEDOT:PSS HTL needs to be substituted by a more suitable electrode interlayer, such as a compact NiO_x layer herein. More importantly, we had developed a process to moderately generate MA gas to treat $CH_3NH_3PbBr_3$ film in a relatively slow reaction way through the unique gas–solid reaction. MA treatment promotes the regrowth of $CH_3NH_3PbBr_3$ crystallites on NiO_x layer following the preferred orientations and significantly enhances the film quality and PL properties. We are aware that the quality of the perovskite active layer would still be the key component to advance the development of perovskite-based hybrid LEDs and could be further improved by the delicate control on the equilibrium condition between a liquid-phase $CH_3NH_3PbBr_3$•xMA intermediate with solid-phase $CH_3NH_3PbBr_3$. Currently, we present a hybrid perovskite-based LED exhibits a peak LE of 15.9 cd A^{-1} biased at 8.5 V, 407.65 mA cm^{-2}, 65 300 cd m^{-2}. The brightness of our result significantly outperforms the state-of-the-art value, which demonstrates the great potential of the approaches we developed in this communication. Such a high brightness implies that the device configuration and the quality of our treated perovskite film can sustain high injection of carriers without failing the device. It is worth noted that our approach can be considered as a feasible fabrication procedure for real application. We believe the NiO_x electrode interlayer and MA treatment method proposed in this manuscript are of the distinctive impact for the future advances in perovskite-based light-emitting diodes, for both stability and efficiency point of view.

Experimental Section

Materials and Sample Preparation: CH_3NH_3Br was synthesized by adding the hydrobromic acid (47%–49%, Alfa Aesar) with the methyl amine (40% aq. solution, Alfa Aesar) in a 250 mL flask with stirring at 0 °C for 2 h. After removing the solvent in a rotary evaporator, CH_3NH_3Br powder was dissolved in ethanol. Later, the diethyl ether was added into the ethanol solution to precipitate CH_3NH_3Br. This process was repeated for three times. CH_3NH_3Br powder was dried in a vacuum oven at 50 °C for 6 h. $PbBr_2$ was synthesized by slowly dropping the sodium bromide (J.T. Baker) aq. solution (0.6 M) into the lead (II) nitrate (J.T. Baker) aq. solution (0.3 M) in a beaker with stirring at room temperature for 1 h. $PbBr_2$ precipitate was washed with ethanol and dried in a vacuum oven at 150 °C for 3 h. $CH_3NH_3PbBr_3$ solution was prepared by mixing 0.306 g of CH_3NH_3Br with 0.963 g of $PbBr_2$ at 1.05:1 ratio in a dimethyl sulfoxide solution (1.7 mL) at 60 °C, stirring for 12 h inside the nitrogen-filled glove box with oxygen and moisture levels <1 ppm.[13]

Device Fabrication: Prior to the device fabrication, the precleaned and -patterned transparent glass/ITO (Ritck Corp., 15 Ω □$^{-1}$) substrates were sequentially cleaned by ultrasonic treatment in detergent, deionized water, acetone, and isopropyl alcohol. After drying, the cleaned substrates were further treated with UV-ozone (Model: 42, Jelight, USA) for 25 min. For the preparation of NiO_x electrode interlayer, the ethylene glycol solution containing 0.5 M nickel formate dihydrate (Alfa Aesar) with 1 molar equivalents of ethylenediamine (Aldrich) was filtered with 0.45 μm nylon filters.[38,40] The solution was spun-cast on glass/ITO substrate at 4500 rpm for 90 s. Then, the substrate was annealed in O_2 atmosphere at 400 °C for 10 min to form the NiO_x electrode interlayer on glass/ITO substrate. NiO_x exhibited an energy level of 5.30–5.40 eV as determined by a scanning Kelvin probe microscopy (Park Systems XE-100). This result agreed with the previous work applying NiO_x electrode interlayer in fabricating perovskite-based hybrid solar cells[40–42] and the observation published elsewhere.[37–39] The conduction band edge levels of NiO_x electrode interlayer were found about 1.70–2.10 eV, respectively, based on the literatures.[37–39] It should be mentioned that the energy levels of NiO_x highly depended on the preparation route. Since NiO_x was a wide band gap semiconductor, there was a big energy barrier in the conduction band edge level (1.70–2.10 eV) of NiO_x with that of $CH_3NH_3PbBr_3$ (3.60 eV) as depicted in Figure 4b to effectively block the transport of electrons reaching the electrode and increase the probabilities for the recombination of opposite charge carriers in $CH_3NH_3PbBr_3$ active layer.

$CH_3NH_3PbBr_3$ perovskite thin film was cast on glass/ITO/NiO_x or glass/ITO/PEDOT:PSS (Baytron P, Bayer AG) substrate by a consecutive two-step spin-coating process at 500 and 3000 rpm for 7 and 90 s, respectively, as illustrated in Figure 1, Step 1. Additionally, 500 μL chloroform solvent was dropped on surface of the precursor film at 60 s during the spin coating.[13] The $CH_3NH_3PbBr_3$ perovskite film was then annealed at 90 °C on a hotplate for 10 min. Afterward, the sample was transferred to the glass vial, containing MA atmosphere. The Step 2 in Figure 1 depicted the process to generate MA gas for MA-$CH_3NH_3PbBr_3$ gas–solid reaction. A solid reaction was adopted to directly blend CH_3NH_3Cl (1.0 g) with KOH (1.0 g) powders in a small vial (4 mL). $CH_3NH_3Cl_{(s)}$ reacted slowly with $KOH_{(s)}$ to generate $MA_{(g)}$, $KCl_{(s)}$, and $H_2O_{(l)}$ at room temperature. Another big vial (50 mL) contained $CaO_{(s)}$ desiccant to absorb H_2O in the above reaction. The glass/ITO/NiO_x/$CH_3NH_3PbBr_3$ substrate was placed upside down in the big vial to react with MA gas coming out from the bottom at room temperature. The MA treatment time was varied from 20 to 100 s. After the treatment, the substrate was removed from the vial (MA atmosphere) to ambient at room temperature. The color or apparent change of the surface morphologies on $CH_3NH_3PbBr_3$ film was not observed by naked eyes during the treatment (0–100 s). Then, the substrate was transferred into a thermal evaporator to deposit TPBI (500 Å, 0.3–0.5 Å s^{-1}), LiF (10 Å, 0.1 Å s^{-1}), and Al electrode (1000 Å, 2 Å s^{-1}) in sequence under a vacuum of 6×10^{-6} Torr. The active area of the device was 0.06 cm^2. Figure 4a depicted the device configuration, composed of glass/ITO/NiO_x/$CH_3NH_3PbBr_3$/TPBI/LiF/Al and Figure 4b diagramed the energy levels of each layer. The $CH_3NH_3PbBr_3$ film had an average thickness of 390 nm, determined by the SEM cross-section image of $CH_3NH_3PbBr_3$ film on the substrate (data not shown here).

Characterization: The SEM images were performed by a S-4700 (Hitachi, Japan) field-emission scanning electron microscope. The

XRD patterns of $CH_3NH_3PbBr_3$ perovskite film was characterized by a Bruker D8 Advance diffractometer (Bragg–Brentano geometry) with Cu Kα-radiation (25 mA, 40 kV) at a scanning speeding of 0.10° s^{-1} and 2θ from 10° to 60°. $CH_3NH_3PbBr_3$ perovskite film was prepared on glass/NiO_x substrate to avoid the interference from ITO for XRD measurement. The current density–brightness–voltage (*J–L–V*) measurements were carried out by a Kiethley 2400 source measuring unit and a Keithley 2000 digital multimeter. The intensity of the EL was recorded by a silicon photodiode (Hamamatsu S2387, Japan) as calibrated by a PR655 spectrophotometer (Photo Research, USA). The measurement of *J–L–V* curves was implemented inside a nitrogen-filled glove box with oxygen and moisture levels <1 ppm. The steady-state PL spectra were taken by a LS-55 fluorescence spectrometer. The excitation wavelength of PL measurement was 365 nm. In order for a comparison of the film morphology of $CH_3NH_3PbBr_3$ perovskite on glass/ITO/PEDOT:PSS and glass/ITO/NiO_x substrate for PL measurement, SEM image (Figure S4, Supporting Information) of $CH_3NH_3PbBr_3$ film on glass/ITO/PEDOT:PSS substrate was added in the Supporting Information. The film prepared by NCP process without MA treatment also exhibited a dense coverage of perovskite layer on glass/ITO/PEDOT:PSS substrate. The grain size was about 200–300 nm and thickness of the film was about 320–350 nm. The fluorescent lifetime was measured using a time-correlated single photon counting (TCSPC) method. The excitation was a pulsed laser diode module (LDH–D-C-485, PicoQuant) with a wavelength of 485 nm and repetition rate of 5 MHz. The nominal pulse width was shorter than 90 ps. The time-resolved signal was detected by a single photon avalanche diode (PDM, Micro Photon Devices) and analyzed by a TCSPC module (PicoHarp, PicoQuant). The total instrument response function (IRF) was smaller than 130 ps and the temporal resolution was better than 10 ps. The lifetimes of the decay curves were determined with a commercial fitting software (FluoFit, PicoQuant).

Supporting Information

Supporting Information is available from the Wiley Online Library or from the author.

Acknowledgements

The author T.-F. Guo would like to thank the MOST of Taiwan (MOST 102-2682-M-006-001-MY3 and MOST 104-2119-M-006-004) and the Asian Office of Aerospace Research and Development (AOARD-14-4012) for financially supporting this research.

Received: June 5, 2016
Revised: June 28, 2016
Published online: August 12, 2016

[1] K. Chondroudis, D. B. Mitzi, *Chem. Mater.* **1999**, *11*, 3028.
[2] K. Chondroudis, D. B. Mitzi, *Appl. Phys. Lett.* **2000**, *76*, 58.
[3] Z.-K. Tan, R. S. Moghaddam, M. L. Lai, P. Docampo, R. Higler, F. Deschler, M. Price, A. Sadhanala, L. M. Pazos, D. Credgington, F. Hanusch, T. Bein, H. J. Snaith, R. H. Friend, *Nat. Nanotechnol.* **2014**, *9*, 687.
[4] Y.-H. Kim, H. Cho, J. H. Heo, T.-S. Kim, N. Myoung, C.-L. Lee, S. H. Im, T.-W. Lee, *Adv. Mater.* **2015**, *27*, 1248.
[5] R. L. Z. Hoye, M. R. Chua, K. P. Musselman, G. Li, M.-L. Lai, Z.-K. Tan, N. C. Greenham, J. L. MacManus-Driscoll, R. H. Friend, D. Credgington, *Adv. Mater.* **2015**, *27*, 1414.
[6] J. Wang, N. Wang, Y. Jin, J. Si, Z.-K. Tan, H. Du, L. Cheng, X. Dai, S. Bai, H. He, Z. Ye, M. L. Lai, R. H. Friend, W. Huang, *Adv. Mater.* **2015**, *27*, 2311.
[7] D. Di, K. P. Musselman, G. Li, A. Sadhanala, Y. Ievskaya, Q. Song, Z.-K. Tan, M. L. Lai, J. L. MacManus-Driscoll, N. C. Greenham, R. H. Friend, *J. Phys. Chem. Lett.* **2015**, *6*, 446.
[8] A. Sadhanala, A. Kumar, S. Pathak, A. Rao, U. Steiner, N. C. Greenham, H. J. Snaith, R. H. Friend, *Adv. Electron. Mater.* **2015**, *1*, 1500008.
[9] G. Li, Z.-K. Tan, D. Di, M. L. Lai, L. Jiang, J. H.-W. Lim, R. H. Friend, N. C. Greenham, *Nano Lett.* **2015**, *15*, 2640.
[10] O. A. Jaramillo-Quintero, R. S. Sanchez, M. Rincon, I. Mora-Sero, *J. Phys. Chem. Lett.* **2015**, *6*, 1883.
[11] A. Sadhanala, S. Ahmad, B. Zhao, N. Giesbrecht, P. M. Pearce, F. Deschler, R. L. Z. Hoye, K. C. Gödel, T. Bein, P. Docampo, S. E. Dutton, M. F. L. De Volder, R. H. Friend, *Nano Lett.* **2015**, *15*, 6095.
[12] S. A. Veldhuis, P. P. Boix, N. Yantara, M. Li, T. C. Sum, N. Mathews, S. G. Mhaisalkar, *Adv. Mater.* **2016**, DOI: 10.1002/adma.201600669.
[13] H. Cho, S.-H. Jeong, M.-H. Park, Y.-H. Kim, C. Wolf, C.-L. Lee, J. H. Heo, A. Sadhanala, N. Myoung, S. Yoo, S. H. Im, R. H. Friend, T.-W. Lee, *Science* **2015**, *350*, 1222.
[14] P. Docampo, J. M. Ball, M. Darwich, G. E. Eperon, H. J. Snaith, *Nat. Commun.* **2013**, *4*, 2761.
[15] N. J. Jeon, J. H. Noh, Y. C. Kim, W. S. Yang, S. Ryu, S. I. Seok, *Nat. Mater.* **2014**, *13*, 897.
[16] M. Xiao, F. Huang, W. Huang, Y. Dkhissi, Y. Zhu, J. Etheridge, A. Gray-Weale, U. Bach, Y.-B. Cheng, L. Spiccia, *Angew. Chem., Int. Ed.* **2014**, *53*, 9898.
[17] P.-W. Liang, C.-Y. Liao, C.-C. Chueh, F. Zuo, S. T. Williams, X.-K. Xin, J. Lin, A. K.-Y. Jen, *Adv. Mater.* **2014**, *26*, 3748.
[18] Q. Chen, H. Zhou, Z. Hong, S. Luo, H.-S. Duan, H.-H. Wang, Y. Liu, G. Li, Y. Yang, *J. Am. Chem. Soc.* **2014**, *136*, 622.
[19] W. Nie, H. Tsai, R. Asadpour, J.-C. Blancon, A. J. Neukirch, G. Gupta, J. J. Crochet, M. Chhowalla, S. Tretiak, M. A. Alam, H.-L. Wang, A. D. Mohite, *Science* **2015**, *347*, 522.
[20] C.-G. Wu, C.-H. Chiang, Z.-L. Tseng, M. K. Nazeeruddin, A. Hagfeldt, M. Grätzel, *Energy Environ. Sci.* **2015**, *8*, 2725.
[21] Y. Rong, Z. Tang, Y. Zhao, X. Zhong, S. Venkatesan, H. Graham, M. Patton, Y. Jing, A. M. Guloy, Y. Yao, *Nanoscale* **2015**, *7*, 10595.
[22] F. X. Xie, D. Zhang, H. Su, X. Ren, K. S. Wong, M. Grätzel, W. C. H. Choy, *ACS Nano* **2015**, *9*, 639.
[23] C. Bi, Q. Wang, Y. Shao, Y. Yuan, Z. Xiao, J. Huang, *Nat. Commun.* **2015**, *6*, 7747.
[24] J. Li, S. G. R. Bade, X. Shan, Z. Yu, *Adv. Mater.* **2015**, *27*, 5196.
[25] S. G. R. Bade, J. Li, X. Shan, Y. Ling, Y. Tian, T. Dilbeck, T. Besara, T. Geske, H. Gao, B. Ma, K. Hanson, T. Siegrist, C. Xu, Z. Yu, *ACS Nano* **2016**, *10*, 1795.
[26] Y. Ling, Z. Yuan, Y. Tian, X. Wang, J. C. Wang, Y. Xin, K. Hanson, B. Ma, H. Gao, *Adv. Mater.* **2016**, *28*, 305.
[27] J. C. Yu, D. B. Kim, E. D. Jung, B. R. Lee, M. H. Song, *Nanoscale* **2016**, *8*, 7036.
[28] Y. Zhao, K. Zhu, *Chem. Commun.* **2014**, *50*, 1605.
[29] Z. Zhou, Z. Wang, Y. Zhou, S. Pang, D. Wang, H. Xu, Z. Liu, N. P. Padture, G. Cui, *Angew. Chem. Int. Ed.* **2015**, *54*, 9705.
[30] Y. Zhou, O. S. Game, S. Pang, N. P. Padture, *J. Phys. Chem. Lett.* **2015**, *6*, 4827.
[31] S. M. Jain, B. Philippe, E. M. J. Johansson, B.-W. Park, H. Rensmo, T. Edvinsson, G. Boschloo, *J. Mater. Chem. A* **2016**, *4*, 2630.
[32] T. Zhao, S. T. Williams, C.-C. Chueh, D. W. deQuilettes, P.-W. Liang, D. S. Ginger, A. K.-Y. Jen, *RSC Adv.* **2016**, *6*, 27475.
[33] S. Pang, Y. Zhou, Z. Wang, M. Yang, A. R. Krause, Z. Zhou, K. Zhu, N. P. Padture, G. Cui, *J. Am. Chem. Soc.* **2016**, *138*, 750.
[34] S. R. Raga, L. K. Ono, Y. Qi, *J. Mater. Chem. A* **2016**, *4*, 2494.
[35] T. Zhang, N. Guo, G. Li, X. Qian, L. Li, Y. Zhao, *J. Mater. Chem. A* **2016**, *4*, 3245.

[36] T. Liu, F. Jiang, J. Tong, F. Qin, W. Meng, Y. Jiang, Z. Li, Y. Zhou, *J. Mater. Chem. A* **2016**, *4*, 4305.
[37] M. D. Irwin, D. B. Buchholz, A. W. Hains, R. P. H. Chang, T. J. Marks, *PNAS* **2008**, *105*, 2783.
[38] A. Garcia, G. C. Welch, E. L. Ratcliff, D. S. Ginley, G. C. Bazan, D. C. Olson, *Adv. Mater.* **2012**, *24*, 5368.
[39] J. R. Manders, S.-W. Tsang, M. J. Hartel, T.-H. Lai, S. Chen, C. M. Amb, J. R. Reynolds, F. So, *Adv. Funct. Mater.* **2013**, *23*, 2993.
[40] J.-Y. Jeng, K.-C. Chen, T.-Y. Chiang, P.-Y. Lin, T.-D. Tsai, Y.-C. Chang, T.-F. Guo, P. Chen, T.-C. Wen, Y.-J. Hsu, *Adv. Mater.* **2014**, *26*, 4107.
[41] W.-C. Lai, K.-W. Lin, T.-F. Guo, J. Lee, *IEEE Trans. Electron Devices* **2015**, *62*, 1590.
[42] W.-C. Lai, K.-W. Lin, Y.-T. Wang, T.-Y. Chiang, P. Chen, T.-F. Guo, *Adv. Mater.* **2016**, *28*, 3290.
[43] J. H. Kim, P.-W. Liang, S. T. Williams, N. Cho, C.-C. Chueh, M. S. Glaz, D. S. Ginger, A. K.-Y. Jen, *Adv. Mater.* **2015**, *27*, 695.
[44] J. H. Park, J. Seo, S. Park, S. S. Shin, Y. C. Kim, N. J. Jeon, H.-W. Shin, T. K. Ahn, J. H. Noh, S. C. Yoon, C. S. Hwang, S. I. Seok, *Adv. Mater.* **2015**, *27*, 4013.
[45] J.-Y. Jeng, Y.-F. Chiang, M.-H. Lee, S.-R. Peng, T.-F. Guo, P. Chen, T.-C. Wen, *Adv. Mater.* **2013**, *25*, 3727.
[46] S. Sun, T. Salim, N. Mathews, M. Duchamp, C. Boothroyd, G. Xing, T. C. Sum, Y. M. Lam, *Energy Environ. Sci.* **2014**, *7*, 399.